

See discussions, stats, and author profiles for this publication at: <https://www.researchgate.net/publication/350773567>

# Aerodynamic effects on an emulated hovering passerine with different wing-folding amplitudes

Article in *Bioinspiration & Biomimetics* · June 2021

DOI: 10.1088/1748-3190/abf6b8

CITATIONS

18

READS

142

2 authors:



[Wei-Han Chen](#)

Georgia Institute of Technology

7 PUBLICATIONS 28 CITATIONS

[SEE PROFILE](#)



[Szu-I Yeh](#)

National Cheng Kung University

20 PUBLICATIONS 163 CITATIONS

[SEE PROFILE](#)

# Aerodynamic Effects on an Emulated Hovering Passerine with Different Wing Folding Amplitudes

Wei-Han Chen<sup>1</sup> and Szu-I Yeh<sup>1,2</sup>

<sup>1</sup> Department of Aeronautics and Astronautics, Tainan, Taiwan

<sup>2</sup> Author to whom any correspondence should be addressed.

E-mail: [siyeh@mail.ncku.edu.tw](mailto:siyeh@mail.ncku.edu.tw)

Received xxxxxx

Accepted for publication xxxxxx

Published xxxxxx

## Abstract

Birds fly with complicated wing kinematics, especially during hovering flight. The detailed aerodynamic effect of wings with higher degrees of freedom remains to be further investigated. Therefore, we designed a novel multiarticulate flapping-wing robot with five degrees of freedom on each wing. This robot is aimed to tackle the more complicated wing kinematics of birds, which are usually difficult to test and analyze. In this study, the robot was programmed to mimic the previously observed hovering motion of passerines and conduct force measurement and PIV experiments. We experimented with two different wing folding amplitudes in this research, one with larger folding amplitude, similar to that of real passerines, and one with only half the amplitude. Kinematics of the robot was verified utilizing direct linear transformation (DLT) which confirmed that the wing trajectories had an acceptable correlation with the desired motion. According to the lift force measurements, 4 phases of the wingbeat cycle were characterized and elaborated through camera images and flow visualization results. We found that the reduction in folding amplitude caused higher negative force during upstrokes, and also induced greater positive force at the initial downstroke through ‘wake capture’ which could increase the vertical oscillation while hovering despite a minor increase in average force production. This phenomenon was not observed during forward flight by previous studies. Our results provide a critical understanding of the effect of wing folding which is required for designing the wing kinematics of future advanced flapping-wing micro aerial vehicles.

Keywords: flapping wing, hovering flight, wing folding, particle image velocimetry

## 1. Introduction

Natural flight has been fascinating and, at the same time, complicated not only in its wing kinematics and also the underlying aerodynamic mechanisms. In recent years, researchers commonly use three different approaches to investigate the aerodynamic performance of flapping-wing flight. The first method is to observe actual flying animals directly inside a controlled experimental environment such as a spacious chamber or a wind tunnel.

Highspeed cameras are commonly used for motion capturing to retrieve the wing kinematics data and are also often used for particle image velocimetry (PIV) for flow visualization. Several studies have experimented with insects and vertebrates such as hawkmoth, pigeons, and hummingbirds (Ros, Badger et al. 2015, Cheng, Tobalske et al. 2016, Warfvinge, KleinHeerenbrink et al. 2017). However, this approach usually requires training animals to fly in relatively confined spaces or some sort of stimulus to encourage the test subject to fly voluntarily while also

ensuring their safety during experiments. This can sometimes be troublesome and could also possibly result in inconsistent measurements. Another approach that is also commonly used is to rely on computational fluid dynamics (CFD) (Tang, Viieru et al. 2008, Trizila, Kang et al. 2011, Zheng, Hedrick et al. 2013). This method provides highly detailed flow structures and velocity information but still usually requires experimental data to validate the accuracy of the computational results (Aono, Chimakurthi et al. 2009, Lankford 2018). The third technique is to construct a dynamically similar robotic model and trying to replicate the actual wing kinematics. Although this allows repeatable and relatively more consistent experiments, reproducing accurate and realistic wing models and wing kinematics have always been a challenge. Therefore, studies have mostly focused on insect flights, which have relatively simple wing planform and kinematics (Lentink and Dickinson 2009, Park and Choi 2012, Van Truong, Byun et al. 2013, Fisher, Ravi et al. 2016). On the other hand, vertebrate flights usually involve wings with complicated geometries and also high degrees of freedom (DOF) which were usually greatly simplified or even ignored during previous related studies (Hubel and Tropea 2010, Crandell and Tobalske 2011).

To further investigate the unsteady aerodynamics of flying vertebrates, a multi-articulated flapping-wing robot has to be constructed. A robotic bat wing was developed with four degrees of freedom to characterized the performance of bats in forward flight (Bahlman, Swartz et al. 2013). The robot was proved to perform accurate kinematic angles with minimal errors. However, only the aerodynamic forces and the power consumption was analyzed. Without the aid of flow visualization, to identify the key aerodynamic mechanisms of flapping with high degrees of freedom could still be painstaking. To thoroughly address this issue, we designed a multi-articulated flapping-wing robot with five degrees of freedom. In addition to conducting force measurements, we also performed PIV flow visualization experiments with this novel flapping robot in a water chamber and characterized several unique aerodynamic events with different flapping kinematics.

## 2. Methods

### 2.1 Wing Kinematics

Flying vertebrates with high DOF wings performs highly dynamic and complicated wing trajectories during hovering which is unique to those of small insects and hummingbirds. Those wings usually feature a two-segmented structure which is composed of an arm section and a hand section that can fold and bend during flight. The

capability of folding and bending their wings holds great benefit in aerodynamic performance. Research has shown that by increasing the bending deflection during upstrokes in forward flight, the negative lift was mitigated and the overall lift production was greatly enhanced (Feshalami, Djavahreshkian et al. 2019). Furthermore, a previous study has pointed out that hovering passerines create additional lift with an unconventional ventral clap mechanism where the two wings fold and come in contact at the end of each downstroke (Chang, Ting et al. 2011). This lift augmentation mechanism was said to compensate for the non-lifting upstroke during asymmetric hovering. Since this hovering motion is one of its kind, we chose to dig deeper into the critical role of wing folding and designed our flapping robot according to one of the most commonly seen passerines in Taiwan, the Japanese White-eye (*Zosterops japonicus*).

The kinematic angles of a hovering Japanese White-eye can be defined with four feature points on each wing, which are the shoulder, wrist, wingtip, and the trailing edge of the wing root as shown in **Figure 1(a)**. These feature points correspond to locations on the flapping robot which are indicated with colored pin markers for easy identification (**Figure 1(b)**). By constructing vectors between different feature points, four key morphological angles shown in **Figure 1(c)** can be defined. First of all, the flapping angle ( $\theta_1$ ) is defined by the angle between the Y-axis and the projection of the vector from the shoulder to the wrist on the Y-Z plane (coronal plane). The second is the sweeping angle ( $\theta_2$ ) which is also formed by the angle between the Y-axis and the same vector as the flapping angle but is projected onto the X-Y plane (transverse plane). The third is the twisting angle ( $\theta_3$ ) which is defined by the angle between the X-axis and the projection of the vector from the shoulder to the trailing edge of the wing root on the X-Z plane (sagittal plane). Last but not least is the folding angle ( $\theta_4$ ), defined by the angle between two vectors where one is formed by the wrist to the shoulder and the other formed by the wrist and the wingtip.

The time histories of these morphological angles within a wingbeat cycle were previously observed and analyzed with high-speed cameras (Chang 2010). The trajectory of each angle was smoothened with an 8<sup>th</sup> order Fourier series which is shown in **Figure 1(d)**. During the characteristic ventral clap motion, which is the transition from downstroke to upstroke, the hand section rapidly morphed from a nearly fully opened position to a retracted position resulted in a large reduction in the folding angle. This not only induces the ventral clap effect but also reduces the effective wing area during upstrokes. To study the effect of the wing -folding amplitude, we experimented

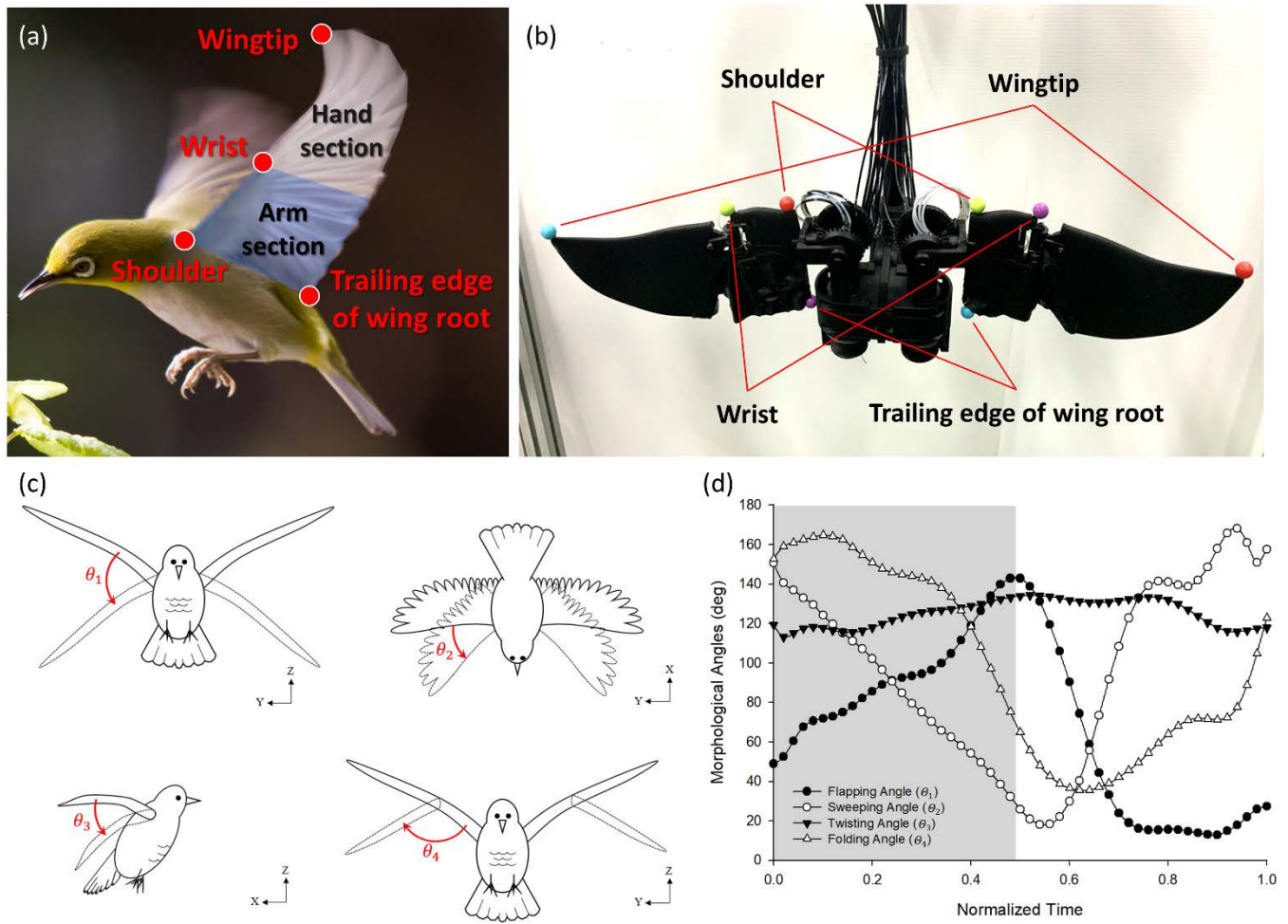


**Figure 1.** (a) Japanese White-eye with the indication of feature points (b) flapping robot and the corresponding pin markers of feature points (c) illustration of the four key morphological angles (d) time history of the four morphological angles with downstroke portion shaded in gray (data adopted from (Chang 2010)).

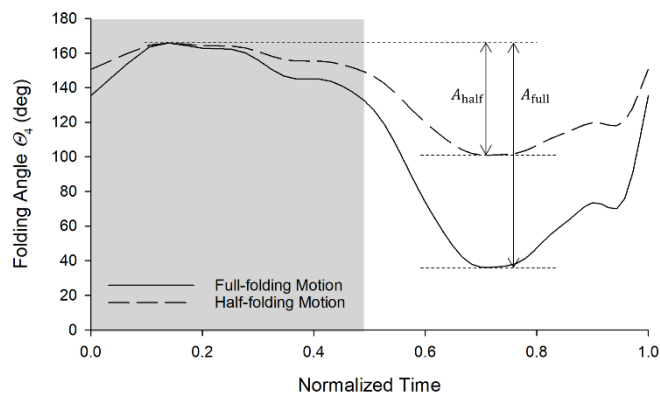


**Figure 2.** Time histories of the two proposed folding kinematics which are the full-folding motion (solid line) and the half-folding motion (dashed line).

with two sets of wing kinematics involving different folding amplitudes (**Figure 2**), one identical with that of real passerines ( $A_{\text{full}} = 130^\circ$ ) and the other with the amplitude reduced by half ( $A_{\text{half}} = 65^\circ$ ). Difference in lift

production was then analyzed with force measurement and flow visualization experiments.

## 2.2 Flapping Robot Design

A multi-articulated flapping-wing robot was designed and constructed to provide high degrees of freedom to mimic the hovering kinematics of passerines and also ensure higher repeatability for experimental purposes. In the process of designing the robot, two important dimensionless parameters, which are the Reynolds number and the reduced frequency ( $k$ ), should be carefully controlled to satisfy flow similarity during experiments. The Reynolds number represents the relation between the inertial force and viscous force which is defined as

$$Re = \frac{\rho V \bar{c}}{\mu} \quad (1)$$

**Table 1.** Dimensionless parameters and the comparison of geometric and kinematic parameters between Japanese White-eye (data adopted from (Chang, Ting et al. 2013)) and our flapping robot.

	Japanese White-eye	Flapping Robot
Reynolds number ( $Re$ )	$3 \times 10^4$	
Reduced Frequency ( $k$ )	0.048	
Wing Length ( $b/2$ )	6.6 cm	15 cm
Maximum wing chord ( $c$ )	3.7 cm	8.4 cm
Flapping Frequency ( $f$ )	24.4 Hz	0.272 Hz
Average wingtip velocity ( $V$ )	9.4 m/s	0.24 m/s

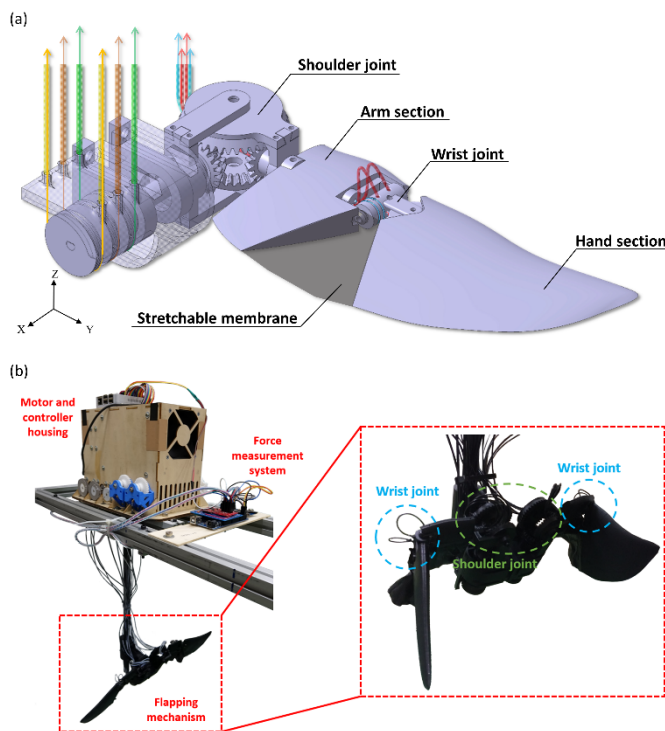


**Figure 3.** (a) Illustration of the flapping mechanism (right wing) where colored lines represent the actuating cable pairs for each degree of freedom (b) Flapping robot assembly including the flapping mechanism, controller housing, and the force measurement system.

where  $\rho$  is the fluid density,  $V$  is the average wingtip velocity,  $\bar{c}$  is the mean aerodynamic chord, and  $\mu$  is the dynamic viscosity of the fluid. On the other hand, the reduced frequency defines the unsteadiness of a flow field which, during hovering flight, can be expressed as

$$k = \frac{f \bar{c}}{2V} \quad (2)$$

where  $f$  is the flapping frequency. For hovering passerines, the averaged Reynolds number and reduced

frequency was observed to be around  $3 \times 10^4$  and 0.048 (Chang, Ting et al. 2013).

The flapping mechanism was designed with a 30 cm total wingspan to reduce sidewall interference inside a rectangular water chamber (1800 mm length  $\times$  800 mm width  $\times$  900 mm height), which has transparent sidewalls for clear observation from all directions during experiments. This results in a model scaling factor of 2.27 compared with the average size of Japanese White-eyes. The required flapping frequency of the robot mechanism was then derived from the above dimensionless parameters, which was 0.272 Hz. The comparison of these parameters between real Japanese White-eyes and the designed flapping robot are listed in **Table 1**.

Similar to the structure of a real vertebrate wing, the proposed mechanism in the study is a two-section design which has an arm section and a hand section (**Figure 3(a)**). The arm section is connected to the main body through a compact 3-DOF coaxial bevel-gear train at the shoulder joint providing flapping, sweeping, and twisting motion. The hand section is attached to the arm section with a 2-DOF wrist joint enabling folding and hand-sweeping movements. The full assembly of the flapping robot consists of a housing for the motors and controller, force measurement system, and the actual flapping mechanism (**Figure 3(b)**). Each degree of freedom is actuated by a NEMA 17 stepper motor inside the housing which is mounted above the water. To transmit the rotary motion from the motor pulleys to each individual joint, 0.35 mm diameter steel cables guided through PTFE (Polytetrafluoroethylene) tubes are routed from the motor housing to the flapping mechanism. This also keeps the flapping mechanism lighter and less bulky which required less power and torque from each actuating motor. The motor pulleys controlling the wrist joint were also built with a reduction ratio of 1.5:1 and 3:1 for the folding motion and the hand-sweeping motion respectively which further reduces the loading on the motors and increases the angular resolution.

Control signals are sent by a Raspberry Pi 3 Model B single-board computer with a custom-written Python code that interprets the desired kinematic angles into the required angles for each degree of freedom. Each motor is controlled through a DRV8825 stepper motor driver chip which is capable of 1/32 microstepping. All electronics, including the power supply, are mounted in the motor and controller housing with sufficient cooling.

### 2.3 Force Measurement

The force measurement system consists of four 2-kgf cantilever load cells attached to the four corners of the

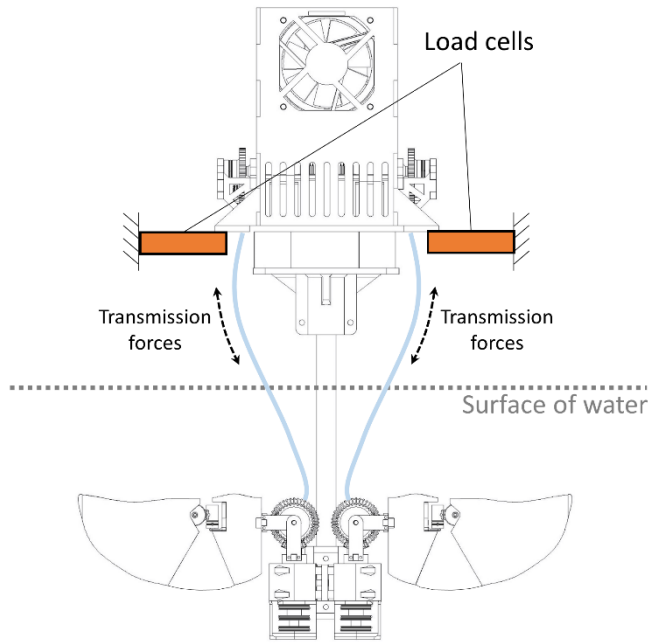


**Figure 4.** Schematic of the force measurement system setup.

motor and controller housing (**Figure 4**). The load cells are connected to an HX711 24-bit high precision analog to digital converter and signal conditioning module. The voltage signal was amplified by the HX711 module with a gain of 128 and the converted digital signal was then captured by an Arduino Mega 2560 development board loaded with custom written firmware which records at a sampling rate of 80 Hz. To calibrate the force measurement system, known weights ranging from 10 to 100 grams were placed on the flapping robot. The calibration result showed that the voltage signal was converted to gram force with great linearity ( $R^2 = 1$ ) within the measuring range. The expected signal noise error is within  $\pm 1.9143$  grams in the measured data under a confidence level of 95% during all measurements by this system.

## 2.4 Flow Visualization

PIV was used to visualize the flow field around the flapping mechanism. A single high-speed camera (Photron Fastcam SA-X; 500 Hz;  $1,024 \times 1,024$  pixels; 12 bits) was used to capture the particle motion illuminated by a laser sheet generated by a solid-state laser (Elforlight HPG-5000; CW; 532 nm; 5 W max power). The seeding particles used were hollow-glass spheres from TSI Inc. which have a nominal diameter ranging from 8 to  $12 \mu\text{m}$ . Laser sheets were lit parallel to the X-Z plane with multiple different stations on the Y-axis ranging from the centerline ( $Y = 0 \text{ mm}$ ) to the wingtip ( $Y = 210 \text{ mm}$ ) with 30 mm increments as illustrated in **Figure 5**. This allows us to observe the sectional velocity field at different locations

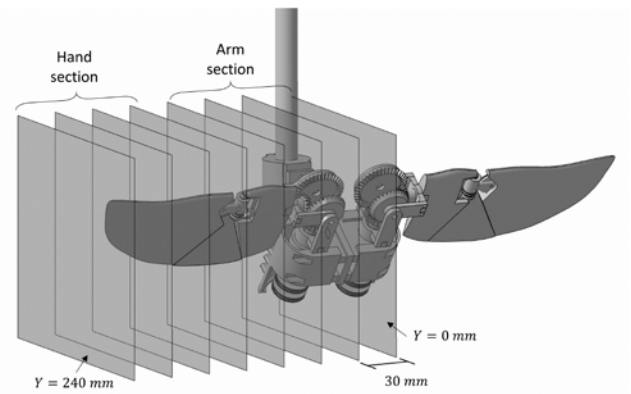


**Figure 5.** Schematic of the flow visualization planes and the spacing between each plane.

along the wingspan for a more detailed understanding of the overall flow structure.

The PIV image processing was done using open-source software – PIVlab, which was written in MATLAB (Thielicke and Stamhuis 2014). The velocity profile was then exported for further image post-processing, which was done in ParaView 5.8.0.

## 3. Kinematic Verification

The kinematic analysis process is necessary to verify that the actual output of the mechanism is as close as possible to what was initially desired. In order to reconstruct the three-dimensional trajectories of the mechanism, a direct linear transformation (DLT) method was implemented, which was commonly used to convert feature points in a set of stereoscopic images into three-dimensional coordinates. This method was also previously used in research to analyze the kinematics of ladybugs during takeoff (George 2011). In this study, three DSLR cameras (Nikon D5600) were used to provide redundancy in case of feature points being blocked at certain angles. The cameras were positioned at locations where it provided minimum distortion due to refraction of the water chamber walls. Video images were captured at 30 frames per second with the shutter speed set to  $1/200$  of a second at a resolution of  $1920 \times 1080$  pixels.

Before the actual experiment, calibration of the cameras was done by capturing a  $150 \times 150 \times 150 \text{ mm}^3$  calibration cube which was made of 2 mm straight copper wire soldered into a grid pattern with a total of 64 calibration points evenly spread across. The calibration results showed that the average positional error of point tracking was less than 2 mm.

After calibration, the wing kinematics of the flapping robot were recorded while submerged in the water chamber prior. Trajectories of all feature points for both cases were recorded and the characteristic kinematic



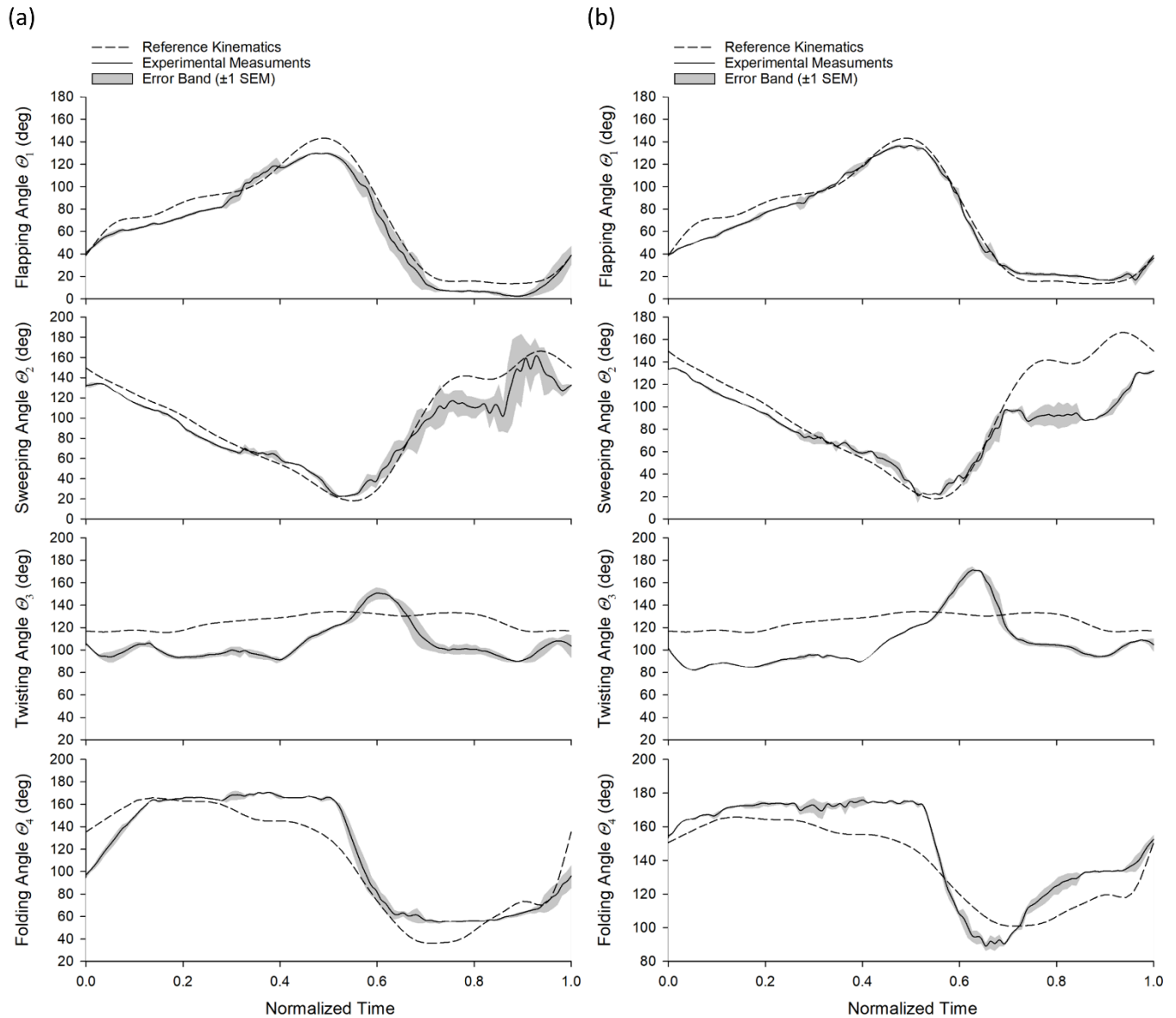


**Figure 6.** Comparison of desired reference kinematics (dashed lines) and the actual camera-captured experimental wing kinematics (solid lines) with  $\pm 1$  SEM error band (a) full-folding motion (b) half-folding motion

angles were reduced from the time history of positional data of each feature point. A custom written MATLAB code was used to automatically track the feature points by identifying the colored pin markers which were shown in **Figure 1(b)**. The markers were only attached to the wings in the kinematic verification experiments.

The camera-captured time histories of kinematic angles were compared with the desired references as shown in **Figure 6** and **Table 2**. The flapping and sweeping angles which are controlled by the shoulder joint showed great tracking performance with high correlation coefficients and small RMS errors. Furthermore, the folding angles also performed equally well in both cases despite being controlled by the wrist joint which had a longer power transmission path. On the other hand, the twisting angle

showed a lower correlation which was most likely due to the inevitable slacks and gaps within the power transmission system making the robot unable to perfectly hold position under the higher load during stroke reversal around  $T = 0.6$ . Nonetheless, the correlation coefficients were greater than 0.5, which still correspond to moderate to high correlation, and the RMS errors were not noticeably higher than other kinematic angles.

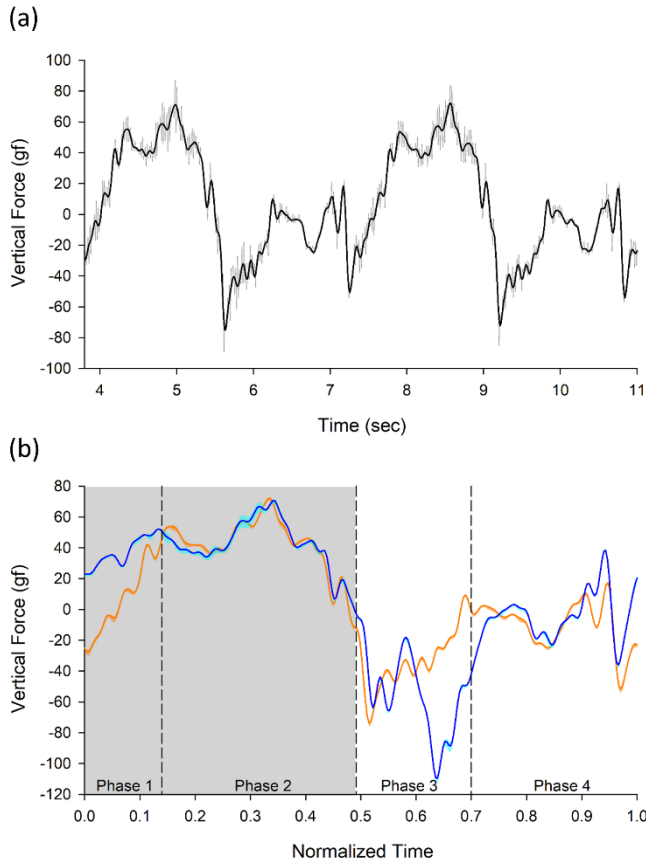
## 4. Results and discussion

### 4.1 Force Measurement and Characterization

The vertical force was recorded over 9 wing beat periods and only 5 periods in the middle were used for analysis to

**Table 2.** Statistical comparison between the desired reference kinematics and the actual wing kinematics of both the full-folding and the half-folding motion

		Flapping Angle	Sweeping Angle	Twisting Angle	Folding Angle
Correlation Coefficient	Full-folding	0.9929	0.9805	0.5151	0.9299
	Half-folding	0.9897	0.9143	0.6042	0.9311
RMS Error	Full-folding	9.53°	14.48°	23.48°	18.57°
	Half-folding	7.12°	26.82°	26.78°	14.47°

**Figure 7.** Force measurement data. (a) Comparison of the raw (thin gray line) and the filtered (thick black line) data of two successive wingbeats of the full-folding motion. (b) Comparison of the averaged vertical force production history between the full-folding (orange) and half-folding (blue) motion with lighter colors indicating the error bands ( $\pm 1$  SEM).

eliminate the effect of the robot starting and stopping. Data were filtered by a lowpass filter with a cutoff frequency of 10 Hz, which removed undesired high-frequency signal noises generated by the amplifier module (Figure 7(a)).

Measurements of the vertical forces within a wingbeat cycle are compared in Figure 7(b) which we can see that the forces produced by the two cases present significant

differences during the initial downstroke and the initial upstroke. According to the unique characteristics of different intervals within a wingbeat cycle, we subdivided them into four distinguishing phases. Phase 1 is the initial downstroke phase, which starts from  $T=0$  to  $T=0.14$ , where the vertical force generated by the half-folding case exceeds that of the full-folding case. Phase 2 then goes from  $T=0.14$  to  $T=0.49$  where both cases generated comparable lift throughout this section of the downstroke. Phase 3 is the folding phase ranging from  $T=0.49$  to  $T=0.7$  during the upstroke right after stroke reversal. This is the most critical phase where the wing kinematics differs the most between the two cases. Phase 4, which had nearly zero averaged vertical force production in both cases, proceeds phase 3 to the end of the wingbeat cycle. The detailed aerodynamic mechanisms underlying these different phases will be further addressed with the aid of PIV images in the subsequent sections.

#### 4.2 Phase 1 – Pre-downstroke

The pre-downstroke phase is the initial section of the downstroke where previous studies showed that the flow field could be highly unsteady due to mechanisms such as added mass or wing-wake interactions (Birch and Dickinson 2003, Liu and Sun 2018). According to Figure 7(b), during this phase, the vertical force generated by the half-folding case reached a near-stable value almost instantly while that generated by the full-folding motion started with a negative value and increased at a significantly slower rate. To understand how the half-folding case was able to rapidly generate lift during the initial downstroke and why the full-folding case generated negative lift initially, we have to take a look at the flow field around the flapping robot.

Flow fields generated by the full-folding and half-folding motion during this phase at different portions are illustrated in Figure 8 for comparison. Throughout phase 1, it can be clearly seen that upward wake and jet flow created by the previous upstroke were significantly



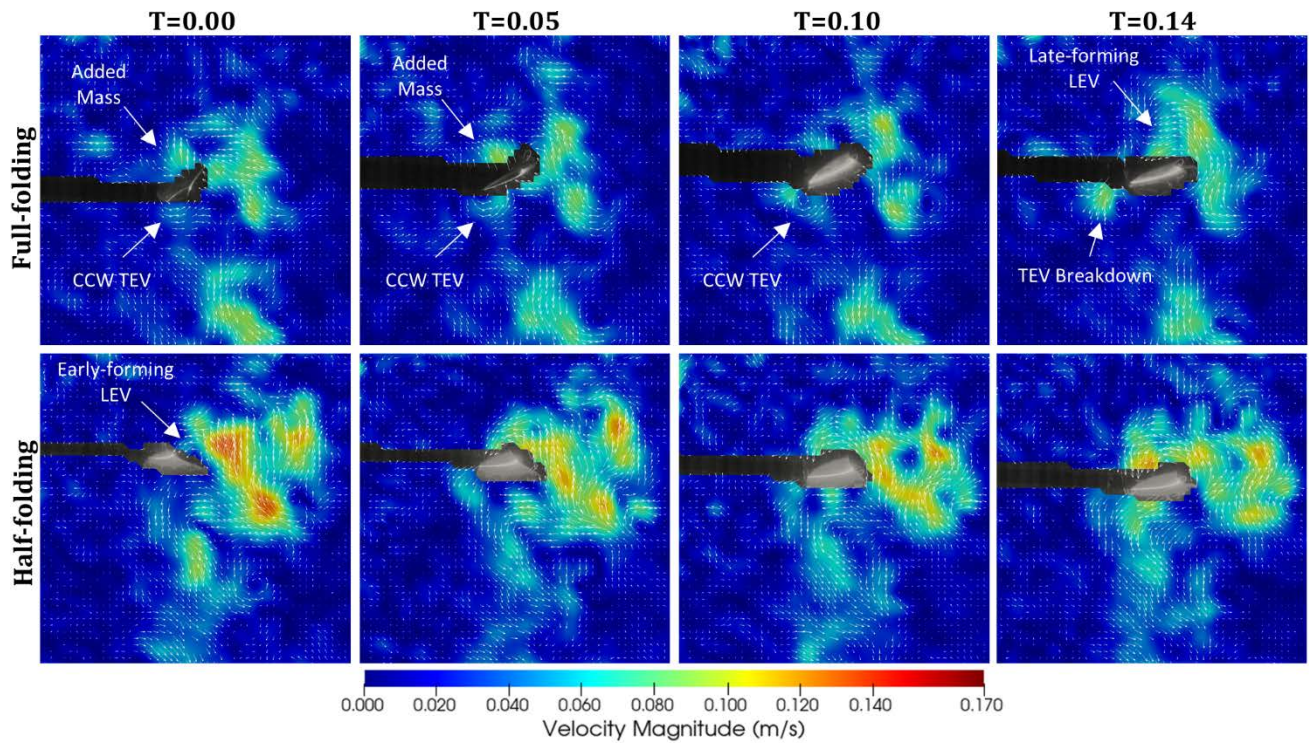


**Figure 8.** Comparison of the sectional flow field from PIV experiment within the pre-downstroke phase at  $Y=150$  mm (hand-section).

greater in the half-folding case. As the downstroke started, the wings flapped through these rearward-flowing wake flow encountering the so-called ‘wake capture’ effect, which, due to the interaction between the previously shed wake and the leading edge of the wing, assisted and accelerated the formation of strong leading-edge vortices (Trizila, Kang et al. 2011). This effect can be observed in **Figure 8** where the upper surface of the wing in the half-folding case already formed visible leading-edge vortices even at  $T=0$ . Consequently, it was able to rapidly generate substantial force at the beginning of each downstroke.

On the other hand, even though there was also visible rearward jet flow created by the full-folding case, it was considerably weaker than that induced by the half-folding case. Furthermore, the initial extending of the folding angle caused the hand section to move in the opposite direction of the downstroke. Instead of benefiting from the jet flow to generate positive force, the extending wing pushed the fluid above it upwards, creating the ‘added mass’ effect in the opposite direction, which can be seen at  $T=0$  and  $T=0.05$  (**Figure 8**). Furthermore, a counterclockwise trailing-edge vortex also provides strong evidence that the hand section was producing negative lift in the initial downstroke. It was not until the unfolding motion slowed down that the wing started to generate positive force. This can also be confirmed by the late-forming leading-edge vortex and the breakdown of the original trailing-edge vortex at  $T=0.14$ .

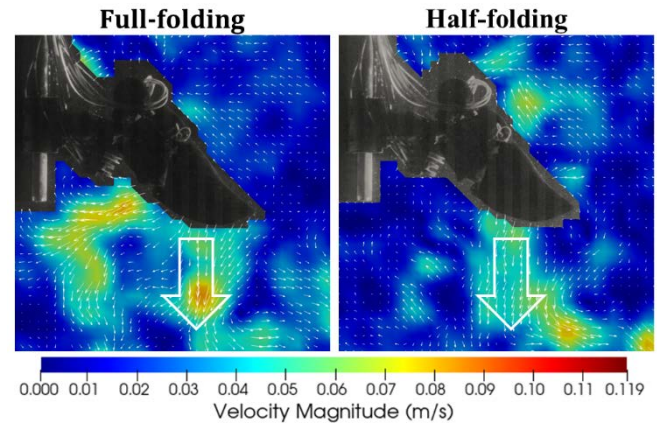


**Figure 9.** Downward jet flow in the symmetry plane ( $Y=0$  mm) resulting from the clap effect near the end of downstroke at  $T=0.47$ .

#### 4.3 Phase 2 – Downstroke

Most of the lift required for hovering flight was produced in the downstroke phase. During this phase, the two cases performed nearly identical wing kinematics, therefore, the force production history was also highly similar. One thing to be noticed, there appeared to be a small spike in force production at  $T=0.47$  right before stroke reversal in both cases, which could indicate a possible ‘clap’ effect that matches the findings in the previous study (Chang, Ting et al. 2013). By examining the velocity field at that moment (**Figure 9**), we found that both cases exhibited a



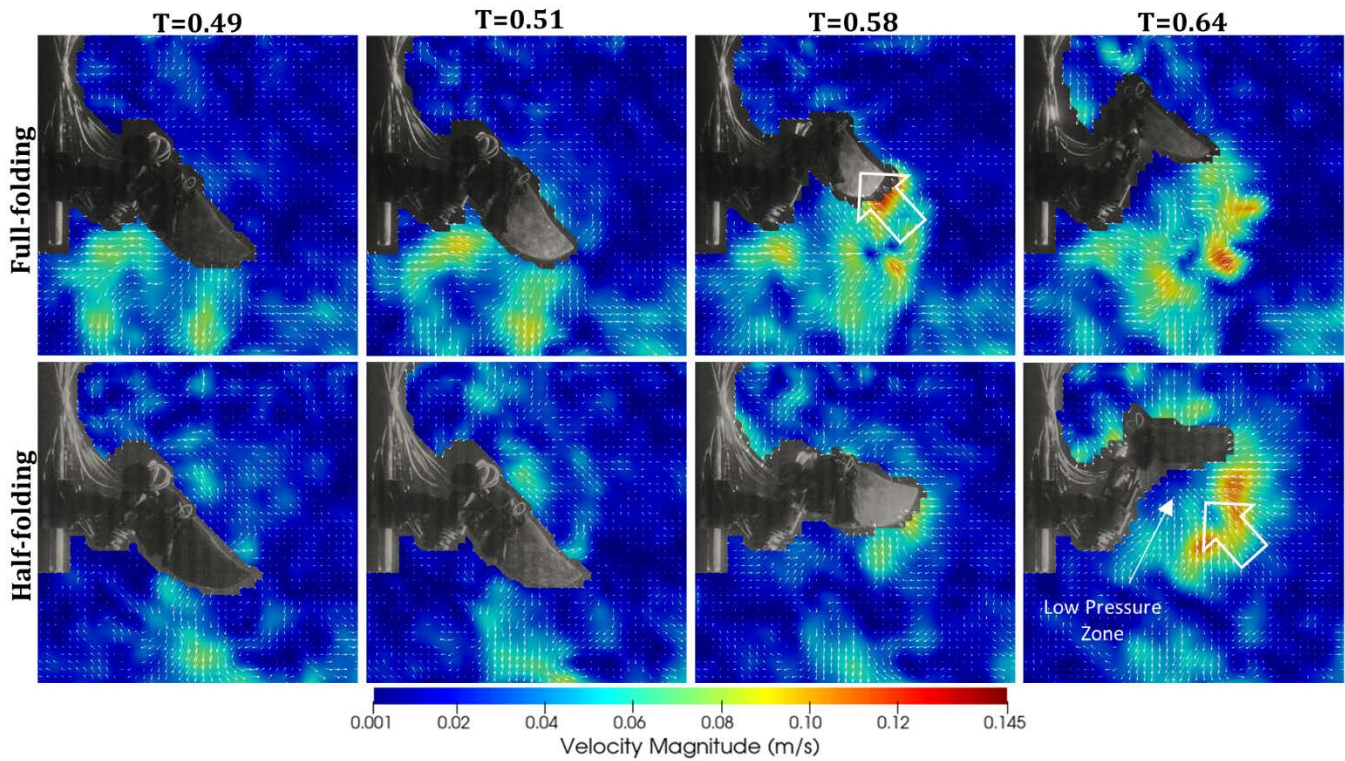


**Figure 10.** Comparison of the sectional flow field in the symmetry plane ( $Y=0$  mm) from the PIV experiment at specific moments within the folding-upstroke phase.

downward jet flow which confirms the existence of a clapping effect that slightly enhanced the vertical force production just before stroke reversal.

#### 4.4 Phase 3 – Folding Upstroke

The main difference between the two kinematic motions comes in the folding upstroke phase where the full-folding case performed a more passerine-like motion and the other followed a trajectory with reduced folding amplitude. To further investigate the relations between wing folding, flow condition, and force production, different moments within this phase were examined with PIV images (**Figure 10**).

During the initial upstroke from  $T=0.49$  to  $T=0.51$ , two cases performed nearly identical motion which led to a similar flow field around the robot. At  $T=0.58$ , wing kinematics started to depart from each other where the full-folding case folded its hand section inwards and the half-folding case still maintained a more extended configuration. From **Figure 10**, we can see that the inward-folding motion of the full-folding case created an upward jet flow with a much higher velocity compared with that created by the other case. As a result, a greater negative vertical force was produced by the full-folding case compared with the half-folding motion at this moment. Following on is the greatest negative force produced by the half-folding motion, which was significantly larger

than the full-folding case at around  $T=0.64$ . At this stage, the upper wing in both cases initiated a rapid sweep-back and pitch-down motion. However, the wings in the full-folding case had already completed the folding process meaning that it had significantly less effective wing area to produce negative force. On the other hand, the extended wing of the half-folding case created a large low-pressure region under the wings which sucked a great amount of fluid inwards and upwards as shown in **Figure 10**. This effect is similar to a ‘fling’ motion, however, in the opposite direction where the trailing edge departs first creating negative vertical force instead.

#### 4.5 Phase 4 – Non-lifting Upstroke

During this phase, the average vertical forces produced by both cases were significantly lower than most other phases in terms of their amplitudes. As the time approaches the end of the wingbeat cycle, wings in both cases rapidly moved rearwards between  $T=0.9$  and  $T=1.0$  which placed the wing in a suitable position for the following downstroke. This also caused the larger fluctuation in the lift at the end of each wingbeat cycle.

#### 4.6 The Overall Effect of All Phases

According to the dynamic scaling law, the equivalent vertical force ( $F_{eq}$ ) during hovering flight in the air can be

**Table 3.** Equivalent averaged vertical force produced by the full-folding motion

	Downstroke		Upstroke	
	Phase 1	Phase 2	Phase 3	Phase 4
Phase-averaged	1.966 gf (28.9%)	11.384 gf (165.0%)	−8.711 gf (−126.2%)	−2.573 gf (−37.3%)
Stroke-averaged	8.666 gf (125.6%)		−5.108 gf (−74.0%)	
Cycle-averaged			1.643 gf (23.8%)	

**Table 4.** Equivalent averaged vertical force produced by the half-folding motion

	Downstroke		Upstroke	
	Phase 1	Phase 2	Phase 3	Phase 4
Phase-averaged	9.979 gf (144.6%)	11.394 gf (165.1%)	−14.528 gf (−210.6%)	−1.221 gf (−17.7%)
Stroke-averaged	10.990 gf (159.3%)		−6.657 gf (−96.5%)	
Cycle-averaged	1.770 gf (25.7%)			

estimated by the scaling of the robot-generated force ( $F_{robot}$ ) with the following equation

$$F_{eq} = F_{robot} \times \frac{\rho_{air} V_{bird}^2 S_{bird}}{\rho_{water} V_{robot}^2 S_{robot}}. \quad (3)$$

From data gathered through the kinematic analysis, the average wingtip velocities of both cases are 0.2537 m/s and 0.2675 m/s respectively. The wing area of the robot is 96.19 cm<sup>2</sup>. According to the previous study, the average wing area, wingtip velocity and body mass of Japanese white-eye are 15.3 cm<sup>2</sup>, 9.4 m/s, and 6.9 g (Chang, Ting et al. 2013). The averaged force contribution of each phase, each stroke, and the entire wingbeat cycle can be calculated where the results are shown in **Table 3** and **Table 4** respectively. The percentages represent the bodyweight ratio of each averaged component.

During downstroke, the half-folding motion greatly benefited from the pre-extended wing and also the ‘wake capture’ effect resulting in nearly identical vertical force production in phase 1 and phase 2. Through the reduced folding amplitude in the half-folding case, the negative lift was increased as expected with a value over 2 times the body weight in phase 3. However, since the folding happened in a relatively short period, the negative effect on the cycle-averaged lift was easily mitigated with the high lift in phase 1 resulting in an even higher cycle-averaged lift.

Although it seems promising that a less-folded wing trajectory could bring larger vertical force, it should be noticed that the variation in lift production, i.e. the peak-to-peak difference in **Figure 7**, is much greater in the less-folding case, which could lead to larger vertical vibrations which are undesirable during hovering. Furthermore, the greater force generated does not necessarily correspond to better flight performance. Generating higher force simultaneously increases the power requirement during flight. A more in-depth study on the power consumption for both wing kinematics is required to determine the optimal point of power efficiency. It should also be noticed that since the flapping robot was designed with a rigid wing surface for simplicity, the aerodynamic performance was expected to be greatly reduced compared with real birds, hence the reason why the cycle-averaged vertical forces for both cases were only around 25% of a bird’s weight.

## 5. Conclusion

The flapping-wing robot constructed in this research provides a platform for kinematic or aerodynamic experiments on flapping wings due to the high DOF and programmable wing trajectories. According to results from the kinematic analysis, the robot is able to perform the two proposed wing kinematics with correlation coefficients over 0.9 for most kinematic angles.

According to the force measurement results, despite the cycle-averaged forces generated by the robot were lower than the bodyweight of a passerine, significant variation in the force production history between the two cases can be clearly seen. The half-folding motion turned out to generated a higher vertical force than that generated by the full-folding case. However, the greater force variation could induce more vertical oscillation during hovering flight. Flight phases such as cruising and hovering require stability and efficiency while taking off and tight maneuvering usually need higher force production to accomplish. Therefore, despite the slightly higher averaged force, a less-folded upstroke during hovering flight might not be the right choice during hovering. Hence why birds opt to fold their wings more aggressively during hovering flight. By selecting suitable wing kinematics in different phases during flight, the overall performance can be greatly increased.

The result in this research demonstrates the aerodynamic effect of different wing folding angles during hovering flight. This is useful while designing the wing kinematics of flapping-wing micro aerial vehicles for different purposes. Further studies on other possible perspectives such as horizontal forces and the total power

requirements are expected to reinforce the understanding of these hovering wing kinematics.

## Acknowledgments

This research is supported by the Ministry of Science and Technology (MOST), R.O.C (Taiwan) project MOST108-2221-E-006-067-MY2. We would also like to thank professor Keh-Chin, Chang for providing crucial test equipment such as the laser and high-speed camera for PIV experiments.

## References

- Aono, H., S. Chimakurthi, C. Cesnik, H. Liu and W. Shyy (2009). Computational modeling of spanwise flexibility effects on flapping wing aerodynamics. 47th AIAA aerospace sciences meeting including the new horizons forum and aerospace exposition.
- Bahlman, J. W., S. M. Swartz and K. S. Breuer (2013). "Design and characterization of a multi-articulated robotic bat wing." Bioinspiration & Biomimetics **8**(1): 016009.
- Birch, J. M. and M. H. Dickinson (2003). "The influence of wing-wake interactions on the production of aerodynamic forces in flapping flight." Journal of Experimental Biology **206**(13): 2257-2272.
- Chang, Y.-H. (2010). Effects of motion kinematics on lift production of a flapping bird-wing. Master Thesis, National Taiwan University.
- Chang, Y.-H., S.-C. Ting, C.-C. Liu, J.-T. Yang and C.-Y. J. E. i. F. Soong (2011). "An unconventional mechanism of lift production during the downstroke in a hovering bird (*Zosterops japonicus*)." Experiments in Fluids **51**(5): 1231-1243.
- Chang, Y.-H., S.-C. Ting, J.-Y. Su, C.-Y. Soong and J.-T. Yang (2013). "Ventral-clap modes of hovering passerines." Physical Review E **87**(2): 022707.
- Cheng, B., B. W. Tobalske, D. R. Powers, T. L. Hedrick, S. M. Wethington, G. T. Chiu and X. Deng (2016). "Flight mechanics and control of escape manoeuvres in hummingbirds. I. Flight kinematics." Journal of Experimental Biology **219**(22): 3518-3531.
- Crandell, K. E. and B. W. Tobalske (2011). "Aerodynamics of tip-reversal upstroke in a revolving pigeon wing." Journal of Experimental Biology **214**(11): 1867-1873.
- Feshalami, B. F., M. Djavareshkian, M. Yousefi, A. Zaree and A. Mehraban (2019). "Experimental investigation of flapping mechanism of the black-headed gull in forward flight." Proceedings of the Institution of Mechanical Engineers, Part G: Journal of Aerospace Engineering **233**(12): 4333-4349.
- Fisher, A., S. Ravi, S. Watkins, J. Watmuff, C. Wang, H. Liu and P. Petersen (2016). "The gust-mitigating potential of flapping wings." Bioinspiration & biomimetics **11**(4): 046010.
- George, R. B. (2011). Design and Analysis of a Flapping Wing mechanism for Optimization, Brigham Young University.
- Hubel, T. Y. and C. Tropea (2010). "The importance of leading edge vortices under simplified flapping flight conditions at the size scale of birds." Journal of Experimental Biology **213**(11): 1930-1939.
- Lankford, J. (2018). Experimental and coupled CFD/CSD investigation of flexible MAV-scale flapping wings in hover. PhD Thesis, University of Maryland.
- Lentink, D. and M. H. Dickinson (2009). "Rotational accelerations stabilize leading edge vortices on revolving fly wings." Journal of Experimental Biology **212**(16): 2705-2719.
- Liu, L. and M. Sun (2018). "The added mass forces in insect flapping wings." Journal of Theoretical Biology **437**: 45-50.
- Park, H. and H. Choi (2012). "Kinematic control of aerodynamic forces on an inclined flapping wing with asymmetric strokes." Bioinspiration & biomimetics **7**(1): 016008.
- Ros, I. G., M. A. Badger, A. N. Pierson, L. C. Bassman and A. A. Biewener (2015). "Pigeons produce aerodynamic torques through changes in wing trajectory during low speed aerial turns." Journal of Experimental Biology **218**(3): 480-490.
- Tang, J., D. Viieru and W. Shyy (2008). "Effects of Reynolds number and flapping kinematics on hovering aerodynamics." AIAA journal **46**(4): 967-976.
- Thielicke, W. and E. Stamhuis (2014). "PIVlab—towards user-friendly, affordable and accurate digital particle image velocimetry in MATLAB." Journal of open research software **2**(1).
- Trizila, P., C.-K. Kang, H. Aono, W. Shyy and M. Visbal (2011). "Low-Reynolds-number aerodynamics of a flapping rigid flat plate." AIAA journal **49**(4): 806-823.
- Van Truong, T., D. Byun, M. J. Kim, K. J. Yoon and H. C. Park (2013). "Aerodynamic forces and flow structures of the leading edge vortex on a flapping wing considering ground effect." Bioinspiration & Biomimetics **8**(3): 036007.
- Warfvinge, K., M. KleinHeerenbrink and A. Hedenström (2017). "The power-speed relationship is U-shaped in two free-flying hawkmoths (*Manduca sexta*)." Journal of the Royal Society Interface **14**(134): 20170372.
- Zheng, L., T. Hedrick and R. Mittal (2013). "A comparative study of the hovering efficiency of flapping and revolving wings." Bioinspiration & biomimetics **8**(3): 036001.